Observation of the spatial growth of self-excited dust-density waves

T. M. Flanagan and J. Goree
Department of Physics and Astronomy, The University of Iowa, Iowa City, Iowa 52242, USA

(Received 12 October 2010; accepted 16 November 2010; published online 7 December 2010)

The growth of a naturally occurring dust-density wave (DDW) is experimentally observed using high-speed imaging. This low frequency wave (~25 Hz) grows in amplitude as it propagates downward through a dusty plasma. The wave's linear growth rate $-k_i$ is measured using a phase-sensitive analysis method. For the conditions studied here, the growth rate increases as gas pressure decreases. At a critical gas pressure, which is observed, a balance between an ion-flow instability and dissipation by neutral gas drag determines a threshold for wave propagation. A linear dispersion relation is derived, taking into account the effects of strong-coupling, to compare to the experiment. © *2010 American Institute of Physics*. [doi:10.1063/1.3524691]

I. INTRODUCTION

Dusty plasma is a suspension of small (micron-size) dust particles in a plasma background (electrons, ions, and neutral gas). In the laboratory, the dust becomes negatively charged by absorbing electrons and ions and are levitated in the plasma sheath's strong electric field. Due to their large mass m_d, dust particles have a much smaller charge-to-mass ratio than electrons and ions. Thus, the time scales of dust dynamics are comparatively much longer and easily observed.

If a dust particle's Coulomb potential energy is larger than its kinetic energy, the dusty plasma is said to be "strongly coupled." In a strongly coupled dusty plasma, the dust particles cannot easily move past one another. Instead, they organize themselves in a structure that is similar to atoms in a solid or a liquid. Due to the dust particle's large negative charge $(-eZ_d)$, mutual dust repulsion dominates their dynamics. In contrast, most electron and ion plasmas are "weakly coupled." With weak coupling, charged particles move easily past one another, like atoms in a gas. In many dusty plasma experiments, the charged dust particles are strongly coupled among themselves, but the electrons and ions are weakly coupled.

Dusty plasma exhibits waves that can be easily observed. Dust motion can be directly imaged with cameras. Dusty plasma is a medium that can support both compressional[1,2] and shear (transverse)[3,4] waves. Waves can be externally excited by electrical[5] or optical[1–4] manipulation. They have a natural phonon spectrum due to random thermal motion.[6] Finally, coherent waves can be excited naturally (i.e., self-excited). The most common example is the dust-acoustic wave,[7,8] also called the dust-density wave.

The dust-density wave (DDW) is a low frequency compressional wave that propagates in dusty plasma,[9] where dust particles participate directly in the wave dynamics. In the DDW, ions and electrons provide the pressure (restoring force), while the dust particles provide the inertia. Experimental studies of the DDW have been performed using a variety of plasmas, both in the laboratory[10–18] and under microgravity conditions.[19–21] The DDW frequency is usually near or below the dust plasma frequency ω_{pd}, which is defined by $\omega_{pd}^2 \equiv n_d e^2 Z_d^2 / m_d \epsilon_o$, where n_d is the dust number density. Typical values for $\omega_{pd}/2\pi$ range from a few hertz to near 100 Hz.

The DDW will often self-excite due to an ion-flow instability. This has been observed both in ground-based experiments[10,14,16,17] and under microgravity.[20,21] The free energy available in the flowing ions[22,23] can drive the DDW to large amplitudes, leading to nonlinear effects.[14,16–18]

The ion-flow instability must compete with dissipation due to neutral gas drag. The wave can be completely damped out at sufficiently high gas pressures, typically about 1 Torr (1 atm=760 Torr). The typical time scale for the damping of dust motion by neutral gas collisions is the Epstein collision rate ν_{dn}, which is defined by $\vec{F}_{\text{drag}} \equiv -m_d \nu_{dn} \vec{V}_d$, where $\vec{F}_{\text{drag}}$ is the drag force experienced by dust due to gas[24] and $\vec{V}_d$ is the relative velocity between dust and gas. For typical micron-size polymer dust particles at a gas pressure of 1 Torr, ν_{dn} is about 100 s^{-1}, which is comparable to a typical dust plasma frequency.

The balance between the ion-flow instability and gas damping determines an instability threshold. This threshold occurs at a critical gas pressure. At the threshold, lowering the gas pressure (or increasing the ion-flow) will cause the wave's onset and subsequent growth, while raising the gas pressure will suppress wave excitation. The instability threshold has been studied previously in experiments[16,25] and theory.[22,23] Below the critical gas pressure, a linear growth of the DDW is predicted.

We know of three previous reports of DDW growth rate measurements. In one case,[26] singular-value decomposition was used to measure the amplitude profile. In two other cases, the spatial variation of dust density[15] or velocity[27] was fitted to an oscillating function with an exponential profile. However, we do not know of any previous measurements of DDW growth rate near the instability threshold. This lack of previous measurements suggests a need to develop a suitable experimental procedure, which we do here.

Here, we report experiments carried out near the critical gas pressure. Using a dust cloud suspended in the sheath of a rf plasma, we reduce the gas pressure in small steps. Using an analysis method developed here yields a measurement of

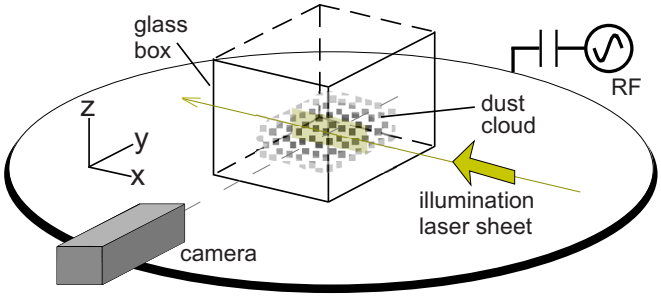

FIG. 1. (Color online) Sketch of the experimental setup. In a radio-frequency argon plasma, dust particles are levitated within the volume of a glass box, forming a dusty plasma. A laser sheet illuminates dust in a vertical plane and the dust cloud is imaged from the side with a digital video camera. For each movie, images are recorded at 500 frames/s for 2.048 s.

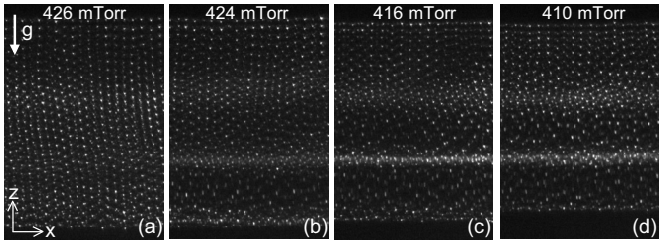

FIG. 2. Single side view images of the dust cloud's central region. Bright spots are individual dust particles. Depending on the gas pressure, energy from a downward ion-flow can couple to dust motion, causing nearly planar compressional waves to be excited and propagate in the $-\hat{z}$ direction. (a) At our starting pressure of 426 mTorr, no wave is observed. Under these stable conditions, dust particles are mainly arranged in horizontal layers. (b) Near a critical pressure of 424 mTorr, the effect of ion-flow barely overcomes gas damping, and a small amplitude wave grows as it propagates downward. The wave fronts are visible in the still image. [(c) and (d)] At lower pressures, ion-flow more effectively couples to dust motion, and the wave grows at a faster rate, reaching larger amplitudes. Each panel shows the same 3.57 mm $\times$ 5.29 mm spatial region. Gravity is directed downward.

the spatial growth rate of the DDW as it propagates downward through the dust cloud.

As our main result, we report growth rate measurements for self-excited dust-density waves. We measure the wave's growth rate for a range of gas pressures near and below the critical gas pressure. This is done using a phase-sensitive analysis method to quantify the wave's amplitude and phase as a function of height in the dust cloud. We find that the growth rate increases as gas pressure decreases. At the lower pressures, the wave amplitude grows faster, eventually reaching a nonlinear amplitude saturation as it traverses the dust cloud.

Additionally, we compare our experimental results to a linear dispersion relation, assuming three fluid components (electrons, ions, and dust), which we adapted to account for strong-coupling among dust particles.

II. EXPERIMENTAL DESIGN

This experiment is designed to observe the growth of self-excited dust-density waves propagating in a strongly coupled dusty plasma. A quantity of about 10^5 spherical polymer dust particles (4.8 μm diameter, 1510 kg/m^3, melamine-formaldehyde) are introduced into an argon plasma using a dust dispenser that is similar to a salt shaker with a single hole. The dust particles are trapped in the plasma within the volume of a glass box. The box has dimensions of 3 cm $\times$ 3 cm $\times$ 3 cm, is open on top and bottom, and rests on an electrode, as sketched in Fig. 1. The electrode is capacitively coupled and powered at radio-frequency (13.6 MHz) with a voltage of 85 V_{pp}, which sustains the plasma through electron-impact ionization. The dust particles are levitated in the plasma sheath, filling a volume near the bottom of the glass box. The sheath's vertical electric field E_z serves two purposes. First, the sheath electric field drives a strong downward ion-flow, which is the DDW's instability energy source. Second, it provides an electric force that balances the dust particles against gravity. The walls of the vertical glass box modify the plasma's natural electric field, providing horizontal dust confinement.[28] This combination of forces confines the dust cloud so that it has many horizontal layers, with overall dimensions of about 22 mm width and 5 mm height.

The dust cloud is illuminated with a vertical laser sheet and is imaged with a digital video camera that views from the side, as sketched in Fig. 1. The camera records images at 500 frames/s at a spatial resolution of $R=76.4$ pixels/mm.

The primary observable in our experiment is dust number density, which we derive from the recorded video images. Regions with higher dust number density scatter more laser light. We verified that the image intensity is linear with dust number density by checking that the camera has a linear response with no offset and by noting that the dust cloud is optically thin (laser light scattered from dust particles is not rescattered in other regions of the dust cloud).

Our imaging setup is designed to detect small variations in dust number density. To reduce the DDW detection threshold, we selected a low-noise 12-bit camera that subtracts background noise levels. Also, we operated the illumination laser at the highest power that would not visibly disturb the dust particles, 0.85 W distributed over a 4 cm high laser sheet.

The experiment begins with a dust cloud levitated in a plasma at a gas pressure of 426 mTorr, which is just high enough that the DDW is not observed. In other words, at our starting pressure the dust cloud is stable. The stable dust cloud's central region is shown in the side view image in Fig. 2(a). Bright spots are individual dust particles. The stable dust cloud is a highly structured strongly coupled dusty plasma. It has many horizontal layers, which are planes of a simple hexagonal lattice, with a vertical alignment of dust due to ion-flow.[29]

Starting near the instability threshold, the instability can be induced by either an increase in ion-flow or a decrease in gas damping (pressure), resulting in a DDW. Unlike the ion-flow, which is difficult to establish at a desired level because it depends on the plasma conditions, the gas pressure is

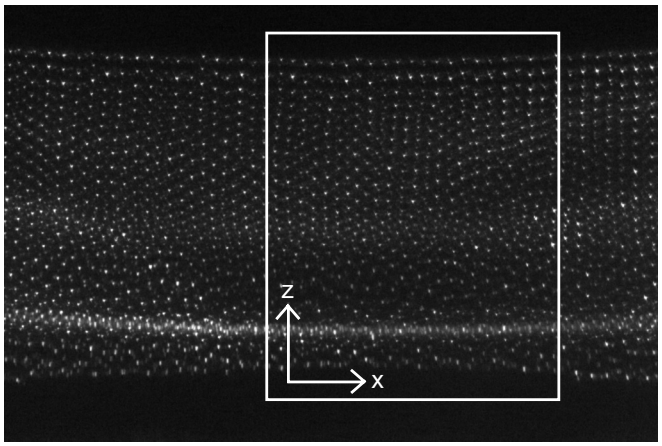

FIG. 3. Image showing the DDW propagating downward through the dust cloud at the critical gas pressure of 424 mTorr. The white rectangle indicates the spatial region that is analyzed. It is the same region that is shown in each panel in Fig. 2. The online reader may view a movie that clearly shows the wave growing as it propagates. This movie clip, which plays at a reduced speed, corresponds to 0.4 s in real time (enhanced online). [URL: http://dx.doi.org/10.1063/1.3524691.1]

easily controlled by the experimenter. Thus, we choose to vary the gas pressure. The critical gas pressure corresponds to the instability threshold and will vary depending on plasma parameters, dust density, and the size of the dust cloud.

To observe wave growth in the dust cloud near the instability threshold, we make observations at a series of gas pressures p that are decreased in steps. In each step, we wait about 1 min to assure that the gas pressure and dust cloud have reached steady conditions. Then, under steady conditions, we record a 1024-frame movie, with a duration of 2 s. Each movie corresponds to one pressure. The steps in gas pressure are in 2 mTorr intervals, which we choose to provide a fine resolution near the instability threshold. We observed planar wave fronts for pressures ranging from the critical pressure down to 404 mTorr, and it is for this range that we recorded data.

III. OBSERVATIONS

We observe nearly planar dust-density waves propagating downward through the dust cloud, Fig. 2. The most compelling evidence of wave propagation is the recorded movie, Fig. 3. The wave is not spatially uniform, but grows in amplitude as it traverses the dust cloud in the $-\hat{z}$ direction.

We observed a critical gas pressure of 424 mTorr in our dust cloud. This was quantified by varying the pressure and finding that a DDW was detectable at 424 mTorr, but not at 426 mTorr, when viewing the movies and by using the image analysis methods we describe later. We term this the *observed* critical gas pressure because its measurement is limited by the detection threshold of our imaging. If we did not have any instrumental limitations, we would presumably measure a somewhat higher critical gas pressure.

A single cropped video frame of the DDW at 424 mTorr is shown in Fig. 2(b). In the upper portion of the cloud, the amplitude of this compressional wave is small enough that individual particles are still easily resolved. As the DDW propagates downward, the wave amplitude grows. In the lower portion, the bright horizontal stripe corresponds to a high-density wave front. There, dust compression is large enough to obscure the particle discreteness.

Reducing the gas pressure further leads to a greater wave amplitude. This trend is shown in the image panels in Figs. 2(c)–2(e). Each panel shows a cropped image from a movie recorded at a different gas pressure. The dust number density, as indicated by image brightness, reaches its greatest values in the wave fronts at lower gas pressures. Next, we develop a quantitative amplitude analysis method, which is used to measure the wave's spatial growth rate.

IV. ANALYSIS

In our analysis, we are only concerned with collective wave properties, and not individual dust particle dynamics. However, we start our analysis with the recorded video images. Instead of tracking the motion of individual dust particles, as is done in some experiments using video microscopy,[29] here we rely on the image intensity and ignore the particle discreteness.

A. Space-time diagrams

For each movie, the basis for our analysis is the space-time diagram, which is a two-dimensional gray scale plot of image intensity. As explained in Sec. II, the image intensity is proportional to dust number density. In a space-time diagram, the vertical axis is vertical position z and the horizontal axis is time t.

A space-time diagram is constructed from recorded images, such as those shown in Fig. 2, as follows. First, each movie frame is cropped to the same spatial region (273 pixels $\times$ 404 pixels), which is indicated by the rectangle in Fig. 3. Since the wave fronts are nearly planar, especially in the region that we analyze, the dust number density varies only with the z coordinate. Second, image intensities are averaged over the ignorable horizontal coordinate x, yielding data for intensities as a function of z (i.e., a vertical profile of intensity). These profiles are produced for each frame (i.e., each time t that an image was recorded). Finally, profiles from each frame are stacked side-by-side, to yield a space-time diagram with time varying on the horizontal axis.

The space-time diagram provides a visual indication of the propagating wave. Wave fronts appear as a sequence of bright and dark stripes. Examples are shown in Fig. 4 for gas pressures of 424 and 410 mTorr and are similar to data at other gas pressures.

In our experiment, the waves are extremely coherent and periodic. This coherency allows us to identify the period, phase velocity, and even wave growth. Phase velocity is

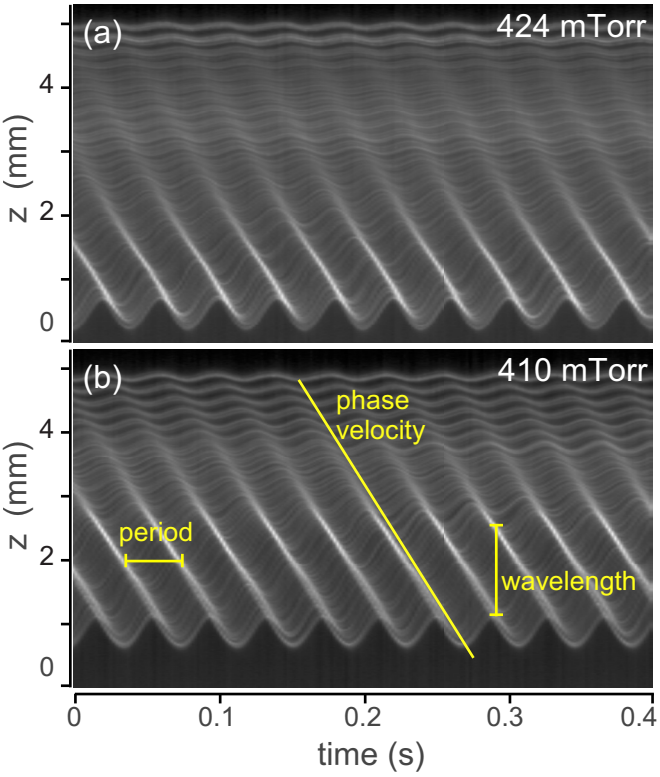

FIG. 4. (Color online) Portions of space-time diagrams for pressures of (a) 424 mTorr and (b) 410 mTorr. Gray scale maps like these are the basis for all our analysis. The bright equally spaced sloped lines indicate wavefronts. Amplitudes grow as the wave propagates downward.

indicated by the slope of the stripes. Amplitude is indicated by the magnitude of the temporal intensity variations. The dominant frequency of the waves is easily quantified as the inverse of the period between stripes, as indicated in Fig. 4(b).

B. Dominant frequency

For the design of our experiment, wave energy is largely concentrated in one dominant frequency f. As an example, for $z>2$ mm at a pressure of 424 mTorr, over 90% of the wave energy is concentrated in a very narrow bandwidth around f, with all other energy at its harmonics.

The dominant frequency f changes only slightly with gas pressure. As gas pressure decreases from 424 to 404 mTorr, f ranges between 24.9 and 26.0 Hz, as shown in Fig. 5.

Unlike some other experiments,[30] here we find that the wave frequency is nearly independent of position in the dust cloud. The dominant frequency f does not vary measurably with z. We found that the spatial invariance of f was true for all gas pressures reported here.

C. Amplitude and phase

To measure the growth of the wave, we develop here an amplitude analysis method that is phase-sensitive. The method is analogous to the principles of an electronic instrument called a lock-in amplifier.[31] This method yields the phase $\phi(z,t)$ and amplitude $A(z,t)$. This method requires that the frequency f be known, that it does not vary with position,

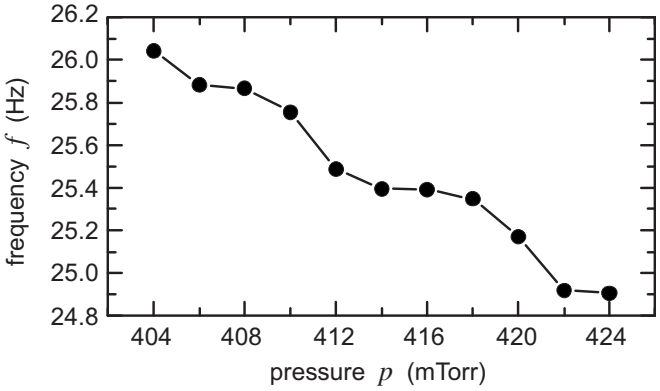

FIG. 5. The dominant frequency f exhibits a slight downward trend with gas pressure. The data points shown are the result of calculating the power spectrum of the space-time diagram.

and that it varies slowly or not at all with time. It also requires a planar wave. The DDW in our experiment satisfies these requirements.

In general, the amplitude analysis method begins by finding the frequency f, and then the following procedure yields the phase ϕ and the amplitude A. The procedure starts with a given waveform $D(\tau)$, which can be, for example, an intensity time series for a given position z in our space-time diagram. We compute the difference between $D(\tau)$ and its time-average $\langle D(\tau)\rangle$. Next, this difference is multiplied by a reference sine wave of frequency f with an adjustable phase β and averaged over N reference wave cycles,

$$I(\beta)=\frac{f}{N}\int_0^{N/f}[D(\tau)-\langle D(\tau)\rangle]\sin(2\pi f\tau-\beta)\mathrm{d}\tau. \quad (1)$$

The resulting integral I depends on the adjustable phase β, which must now be selected. We vary β to find the value $\beta_{\max}$ that maximizes $I(\beta)$. We interpret $\beta_{\max}$ as the phase ϕ and $I(\beta_{\max})$ as the amplitude A.

For our experiment, we apply this method to the intensity data in our space-time diagrams, yielding the amplitude $A(z,t)$ and phase $\phi(z,t)$. The inputs required for Eq. (1) are f, N, and $D(\tau)$. To determine the frequency f, we use a power spectrum of the space-time diagram. We partition each space-time diagram into "sections" that are $M=15$ pixels in vertical space and $N=5$ wave periods in time. These sections define the spatial (M/R) and temporal resolution (N/f) of our amplitude and phase results. Within each section, we average the M pixel intensities at each time, resulting in the time series $D(\tau)$.

We apply Eq. (1) to each section in the space-time diagram, yielding the full spatial and temporal dependence of the amplitude $A(z,t)$ and phase $\phi(z,t)$. The spatial profiles $A(z)$ and $\phi(z)$ are calculated by moving the partitioned section throughout the vertical extent of the dust cloud in one-pixel steps, calculating A and ϕ at each step. These spatial profiles are repeated at time intervals separated by the temporal resolution N/f. To choose a value for N, we require

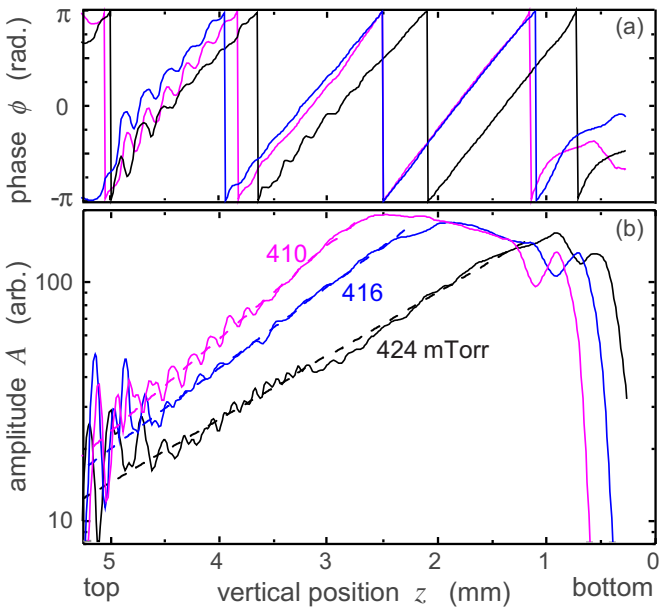

FIG. 6. (Color online) Spatial profiles of the dust-density wave's (a) phase $\phi(z)$ and (b) amplitude $A(z)$ for three gas pressures. These profiles are computed using the method described in Sec. IV C. The growth is more rapid at lower gas pressures. Amplitude data (plotted log-linear) reveal exponential growth as the wave propagates downward. We quantify the growth rate by fitting the profiles to an exponential (straight dashed lines).

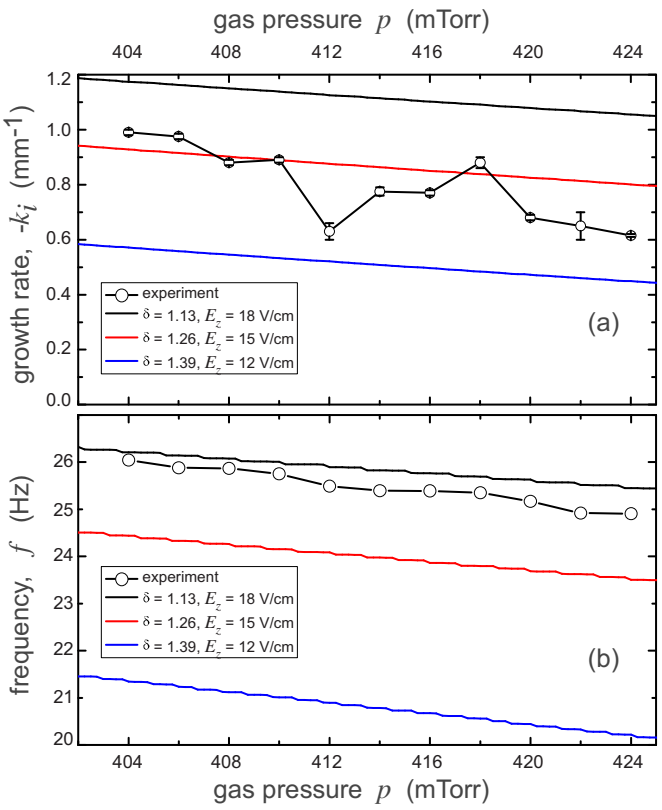

FIG. 7. (Color online) Variation with gas pressure of (a) spatial growth rate $-k_i$ and (b) frequency f. The errors in the experimental $-k_i$ measurements shown here reflect variations due to the arbitrary choice of the range of z used in fitting the amplitude profile. Solid curves for the theory assume experimental parameters listed in Table I (Appendix).

that N/f is at least as long as the time required for the wave to transit the entire dust cloud. For our experimental parameters, we choose $N=5$, so that our time resolution is typically 0.2 s, and our movies of duration of 2 s yield ten spatial profiles.

V. GROWTH RATE RESULTS

Spatial profiles of phase $\phi(z)$ and amplitude $A(z)$ are indicators of wave propagation and growth, respectively, and are shown in Fig. 6 for three different gas pressures. The phase ϕ varies linearly with z, indicating a propagating wave. The direction of wave propagation is downward, as indicated by a phase that increases as position z decreases, as shown in Fig. 6(a). The phase varies over about 6π radians, indicating that there are about three wavelengths in the vertical extent of the dust cloud. At small wave amplitudes near the top of the dust cloud (large z), there is some ripple in $\phi(z)$, which is an artifact of horizontal layering of dust.

As the DDW traverses the dust cloud, its amplitude grows exponentially with a well-defined spatial growth rate. The growth rate $-k_i$ is measured by fitting the amplitude profile to an exponential. Semilog plots of $A(z)$ along with their exponential fits are shown in Fig. 6(b). As an example of our measurements, near the instability threshold at $p=424$ mTorr, the slope of the dashed line in Fig. 6(b) gives a measured growth rate of 0.61 mm^{-1}. The wave amplitude grows exponentially throughout most of the dust cloud, but not all of it. The growth saturates, reaching a maximum amplitude in the lower region of the dust cloud. To avoid any effect of this saturation in our measurements of $-k_i$, we fit data only up to 0.3 mm above the position of maximum amplitude.

There is no evidence of a reflected wave at the dust cloud's bottom edge, where the amplitude quickly drops. Reflected waves do not grow due to the instability because they propagate in the opposite direction of the flowing ions. Instead, they are only damped by gas friction. Using the known Epstein collision rate ν_{dn} and the measured phase velocity v_{ph} of the downward-propagating wave, we estimate that the upward-propagating reflected wave would be completely damped out in a very short distance $v_{ph}/\nu_{dn} \approx 0.3$ mm, comparable to one or two dust particle spacings.

As our chief result, measurements indicate that the growth rate of the downward-propagating wave increases as the neutral gas pressure is decreased. All measured growth rates $-k_i$ are plotted as open circles versus gas pressure p in Fig. 7(a). Regardless of how the DDW is theoretically modeled, this trend is expected. Reducing gas pressure tends to promote wave growth for two reasons. A lower gas pressure reduces neutral gas damping and it increases the ion-flow velocity. The ion-flow increases because mobility is inversely proportional to gas pressure.

All the growth rate results reported in Fig. 7(a) are for the dust cloud's upper region, where nonlinear effects are

weak. As the wave traverses the dust cloud, the amplitude grows large and saturates in the dust cloud's lower region. Saturation of the wave's growth in the lower region is an indicator of nonlinearity. We will study DDW nonlinearities in another paper, based on a separate experiment.

VI. FLUID MODEL FOR LINEAR WAVES

Wave dispersion relations in the case of strong Coulomb coupling are more difficult to derive than for weak coupling. For the DDW, there have been several previous theoretical derivations, as reviewed by Piel and Melzer.[32] Generally, they require modeling the strongly coupled plasma's microscopic structure, which creates local Coulomb potential wells between particles. Several approaches have been adopted to model how compressional wave motion is influenced by these local potentials. Rosenberg and Kalman[33] used the quasilocalized charge approximation, which is suited for disordered structures such as liquids, to derive a dispersion relation. Kaw and Sen[34] used the generalized hydrodynamic description to include strong-coupling effects among the dust particles in analyzing their elastic and viscous response to wave motion. Murillo[35] used dynamical local field corrections to account for strong-coupling effects. In the dispersion relation that we derive next, we will use a simplified model for our dust cloud's microscopic structure.

At small amplitudes, dust-density waves are commonly described using a linear wave theory with three fluid components (electrons, ions, and dust).[9,20] Here, we develop a similar model, except that we also include an approximation of strong-coupling among the dust particles. In order to compare to our experimental observations, our model includes flowing ions and gas drag, which can excite and damp waves, respectively.

Assuming planar waves propagating in an infinite uniform plasma, the electrostatic dispersion relation is

$$\epsilon(k,\omega) \equiv 1 + \chi_e + \chi_i + \chi_d = 0, \tag{2}$$

where χ_e, χ_i, and χ_d are the susceptibilities for electrons, ions, and dust, respectively. Equation (2) is a statement of Poisson's equation. We assume the wave number k is real, but we allow the frequency ω to be complex. For each fluid component, there is also a continuity equation and a momentum equation.[9,20]

The electron and ion susceptibilities are derived in the usual way for weakly coupled plasmas, from the linearized continuity and momentum equations. Because dust-density waves have a very low frequency, the wave frequency ω can be ignored in both χ_e and χ_i. We assume an ideal-gas equation of state for the weakly coupled electrons and ions, so that their fluid pressures are $P_{e(i)}=n_{e(i)}k_BT_{e(i)}$, where $n_{e(i)}$ and $T_{e(i)}$ are the number density and temperature of electrons or ions. For the electron susceptibility χ_e, we assume the electrons have only random thermal motion with no bulk flow, so that

$$\chi_e = (k\lambda_{D_e})^{-2}, \tag{3}$$

where k is the wave number and $\lambda_{D_e}=(\epsilon_o k_B T_e/n_e e^2)^{1/2}$ is the electron Debye length. For the ion susceptibility χ_i, we include the flow of ions with velocity U_0 parallel to the wave vector. We also include a drag force on ions due to collisions with neutrals, at a collision rate ν_{in}, yielding

$$\chi_i = \frac{\omega_{pi}^2}{(v_{T_i}^2 - U_o^2)k^2 + i\nu_{in}U_o k}. \tag{4}$$

This expression has both real and imaginary parts. It will be significant later, when we discuss instability, that the imaginary part of χ_i is due to the ion-flow U_o. Here, $\omega_{pi}=(n_i e^2/\epsilon_o m_i)^{1/2}$ is the ion plasma frequency and $v_{T_i}=(k_B T_i/m_i)^{1/2}$ is the ion thermal velocity.

The dust susceptibility χ_d is modeled differently than the electrons and ions for two reasons. First, since the massive dust particles provide the wave's inertia, our expression for χ_d must include the wave frequency ω. Second, the dust particles are strongly coupled, unlike the electrons and ions, which are weakly coupled.

In our fluid model, the effects of strong-coupling appear only in the dust pressure gradient term $-\vec{\nabla}P_d$ of the dust momentum equation. The dust pressure gradient term is different from $-\vec{\nabla}(n_d k_B T_d)$ for the weakly coupled case, where an ideal-gas equation of state is assumed. For the strongly coupled dust, pressure arises mainly from Coulomb interactions with nearby charged dust particles.

To use the fluid model, we must find an appropriate expression for $-\vec{\nabla}P_d$. It is no trivial matter to model P_d for strongly coupled plasmas because the equation of state depends on the exact microscopic structure, for example, a bcc versus a fcc lattice for a solid or something more disordered for a liquid.

One approach for incorporating strong-coupling effects in the dust momentum equation is to rewrite $-\vec{\nabla}P_d$ using the sound speed C_l.[36,37] The required physics in the equation of state, for our purposes, must be provided by a model for the sound speed. We make use of $C_l^2=\partial P_d/\partial(m_d n_d)$, which assumes that the dusty plasma is isentropic. The error introduced by the isentropic assumption is no larger than other uncertainties that will enter into our approximations below. Thus, we account for strong-coupling among dust particles by using $-\vec{\nabla}P_d=-m_d C_l^2\vec{\nabla}n_d$ in the dust momentum equation.

The dust susceptibility is then found by combining the continuity equation and the equation of motion for dust, making use of the above expression for $-\vec{\nabla}P_d$, so that

$$\chi_d = \frac{\omega_{pd}^2}{C_l^2 k^2 - \omega(\omega + i\nu_{dn})}. \tag{5}$$

Here, ω_{pd} is the dust plasma frequency. The neutral gas damping rate ν_{dn} entered the derivation of Eq. (5) in the dust equation of motion.

The dispersion relation can be algebraically solved for the complex frequency $\omega=\omega_r+i\omega_i$. Noting that χ_e and χ_i are independent of ω, we find by substituting Eq. (5) into Eq. (2),

$$\omega(k) = -i\frac{\nu_{dn}}{2} + \sqrt{\frac{\omega_{pd}^2}{1+\chi_e+\chi_i} + C_l^2k^2 - \frac{\nu_{dn}^2}{4}}. \quad (6)$$

Strong-coupling effects appear in Eq. (6) in the term $C_l^2k^2$. For comparison, in the traditional weakly coupled case, the term $C_l^2k^2$ is replaced by $(k_BT_d/m_d)k^2$ in Eq. (6).

We now assess the dispersion relation in Eq. (6) to determine the conditions for an instability. The DDW is unstable if $\omega_i>0$, stable if $\omega_i<0$, and critically stable if $\omega_i=0$. We see that an instability (and thus a self-excited DDW) is possible in our model by examining the two terms on the right-hand side of Eq. (6). The first term, arising from gas damping, is a purely negative imaginary number. However, the square-root term, arising from all the charged constituents, has both real and imaginary parts. The imaginary part of the square-root term, which comes from the $i\nu_{in}U_ok$ term in Eq. (4), is positive when the direction of wave propagationis aligned with the ion-flow. Thus, gas damping tends to stabilize the wave, while ion-flow tends to promote an instability that drives a DDW propagating parallel to the ion-flow. Since ν_{dn} is proportional to gas pressure p, we expect that our theoretical model can predict a critical gas pressure where $\omega_i=0$. The accuracy of this prediction is limited by the approximations of the dust equation of state, among other things.

We expect that a self-excited wave will be dominated by the most unstable k-mode. In other words, the k-mode with the highest growth rate ω_i is the mode that should be observed. Thus, for our theoretically predicted mode, we select the k that maximizes the imaginary part of Eq. (6).

In solving our dispersion relation, we assumed a real k and a complex ω. However, in our experiment, we measure a spatial growth rate $-k_i$. If we wish to compare to experimental results with a real ω and a complex k, we will use the approximate expression[26] $\omega_i\approx-k_iv_g$. Here, $v_g=\partial\omega_r/\partial k_r$ is the DDW group velocity, which can be calculated from Eq. (6).

To use Eq. (6) requires choosing an expression for C_l, which could, in principle, be derived for any particular microscopic structure. In Sec. VII, for simplicity, we use an expression[37] for C_l intended for the long-wavelength limit of a one-dimensional chain of particles interacting with a Yukawa potential and assume a screening parameter $\kappa=1$.

VII. EXPERIMENT VERSUS LINEAR WAVE THEORY

We will now examine whether the linear wave theory predicts our experimental results: a trend that growth rate diminishes with increasing gas pressure and a critical gas pressure for the instability. We will make rough quantitative estimates of the growth rate predicted by the model and compare to the experiment.

The theoretical and experimental growth rates are compared in Fig. 7(a) as a function of gas pressure. We note that they exhibit the same trend: the growth rate diminishes with gas pressure. We do not expect exact numerical agreement for several reasons: the theory is purely linear, some experimental parameters required in the theory are not precisely known (see Appendix), and the theory is for an unbounded plasma. The finite 5mm height of the experimental dust cloud prevents detecting any $-k_i<0.2$ mm^{-1}. Theoretical results are shown for several representative estimates of experimental parameters.

Earlier, we found in the experiment that the frequency f diminishes with gas pressure (Fig. 5). This trend is also exhibited by the theory, as shown in Fig. 7(b).

The theoretical model also predicts a critical gas pressure, just as we observe in the experiment. Extrapolating the three theoretical curves in Fig. 7(a) to higher gas pressures, the curves all have zeroes, which correspond to the theoretical critical gas pressure. For the curves in Fig. 7(a), the theoretical critical pressure is in the range 530–710 mTorr, which is higher than the observed critical gas pressure of 424 mTorr.

VIII. SUMMARY

In a laboratory dusty plasma experiment, we observe the spatial growth of self-excited dust density waves. By observing our dust cloud at various gas pressures, we find that a DDW self-excites at a critical gas pressure due to an ion-flow instability that just overcomes neutral gas damping. At pressures near and just below this critical gas pressure, the wave amplitude grows as it propagates through the dust cloud.

As our main result, we measure the spatial growth rate $-k_i$ of dust-density waves near the instability threshold. To do this, we developed a method of measuring amplitude that is phase-sensitive. This method yields a spatial profile of the wave's amplitude and phase. Fitting the amplitude profile to an exponential yields the growth rate $-k_i$. Our results reveal a trend that the growth rate increases as gas pressure decreases. The frequency exhibits the same trend.

Additionally, we compare our experimental results with a linear wave theory that includes the effects of strong-coupling. The theory shows the same trends that growth rate and frequency decrease as gas pressure increases. As expected, the theory predicts a critical gas pressure for a self-excited DDW. The theory's assumption of small-amplitude waves is most likely to be valid near the instability threshold, which is where we performed the experiment.

ACKNOWLEDGMENTS

The authors would like to thank F. Skiff and R. L. Merlino for helpful discussions. This work was supported by NASA contracts NNX07AD22G and NNX10AR55G and NSF contract 0903501.

TABLE I. Input parameters for linear wave model.

Parameter	Estimate value	Expression	Comment
MEASURED			
n_e	2×10^8 cm^{-3}		Langmuir probe
T_e	6–8 eV		Langmuir probe
T_i	1/40 eV		room temperature
n_d	1.2×10^5 cm^{-3}		image analysis
Cloud height	4.5–5.0 mm		image analysis
KNOWN			
m_dg	8.6×10^{-13} N		manufacturer specifications
ASSUMED			
κ	1		Arp *et al.*[a]
δ	1.26 ± 0.13		Liu *et al.*[b]
COMPUTED			
ν_{dn} (s^{-1})		$255\delta p$ (Torr)	Liu *et al.*[b]
$-E_z$	15 ± 3 V/cm		T_e/(cloud height)
μ_+ (cm^2/V s)		$1052/p$ (Torr)	mobility from Frost[c]
U_o (cm/s)		$1052E_z$ (V/cm)/p (Torr)	μ_+E_z
ν_{in} (s^{-1})		2.34×10^7p (Torr)	$e/(m_i\mu_+)$
Z_d	4000		$eZ_dE_z=m_dg$
C_l	23 mm/s		equation (5) of Wang *et al.*[d]
SIMULATED			
n_i	6×10^8 cm^{-3}		fluid simulation[e]

[a]Reference 28.
[b]Reference 38.
[c]Reference 39.
[d]Reference 37.
[e]Reference 40.

APPENDIX: ESTIMATES OF EXPERIMENTAL PARAMETERS

Here we present estimates of some experimental parameters to test the linear wave theory, in Sec. VII. The two input parameters that have the largest effect on the theoretically predicted growth rates are the vertical electric field E_z (since $E_z\propto U_o$, the ion-flow instability source) and the Epstein collision rate ν_{dn} (since it directly affects wave damping). Thus, in Table I, we provide an uncertainty range for estimates of E_z and ν_{dn},[38] along with justification for their estimated values. Also in Table I, we list estimates of all other input parameters in the theoretical model. We have verified that our estimates of E_z, n_e, n_i, T_e, and T_i are reasonable by performing a fluid simulation of our experiment's entire discharge.[40]

[1]S. Nunomura, J. Goree, S. Hu, X. Wang, and A. Bhattacharjee, Phys. Rev. E **65**, 066402 (2002).
[2]V. Nosenko, K. Avinash, J. Goree, and B. Liu, Phys. Rev. Lett. **92**, 085001 (2004).
[3]S. Nunomura, J. Goree, and D. Samsonov, Phys. Rev. Lett. **84**, 5141 (2000).
[4]V. Nosenko, J. Goree, Z. W. Ma, and A. Piel, Phys. Rev. Lett. **88**, 135001 (2002).
[5]A. Melzer, M. Klindworth, and A. Piel, Phys. Rev. Lett. **87**, 115002 (2001).
[6]S. Nunomura, J. Goree, S. Hu, X. Wang, A. Bhattacharjee, and K. Avinash, Phys. Rev. Lett. **89**, 035001 (2002).
[7]A. Barkan, R. L. Merlino, and N. D'Angelo, Phys. Plasmas **2**, 3563 (1995).
[8]C. Thompson, A. Barkan, N. D'Angelo, and R. L. Merlino, Phys. Plasmas **4**, 2331 (1997).
[9]N. N. Rao, P. K. Shukla, and M. Y. Yu, Planet. Space Sci. **38**, 543 (1990).
[10]V. E. Fortov, A. G. Khrapak, S. A. Khrapak, V. I. Molotkov, A. P. Nefedov, O. F. Petrov, and V. M. Torchinsky, Phys. Plasmas **7**, 1374 (2000).
[11]E. Thomas, R. Fisher, and R. L. Merlino, Phys. Plasmas **14**, 123701 (2007).
[12]P. Bandyopadhyay, G. Prasad, A. Sen, and P. K. Kaw, Phys. Lett. A **368**, 491 (2007).
[13]P. Bandyopadhyay, G. Prasad, A. Sen, and P. K. Kaw, Phys. Rev. Lett. **101**, 065006 (2008).
[14]J. Heinrich, S.-H. Kim, and R. L. Merlino, Phys. Rev. Lett. **103**, 115002 (2009).
[15]V. E. Fortov, A. D. Usachev, A. V. Zobnin, V. I. Molotkov, and O. F. Petrov, Phys. Plasmas **10**, 1199 (2003).
[16]M. Schwabe, M. Rubin-Zuzic, S. Zhdanov, H. M. Thomas, and G. E. Morfill, Phys. Rev. Lett. **99**, 095002 (2007).
[17]C.-T. Liao, L.-W. Teng, C.-Y. Tsai, C.-W. Io, and I. Lin, Phys. Rev. Lett. **100**, 185004 (2008).
[18]L.-W. Teng, M.-C. Chang, Y.-P. Tseng, and I. Lin, Phys. Rev. Lett. **103**, 245005 (2009).
[19]S. Khrapak, D. Samsonov, G. Morfill, H. Thomas, V. Yaroshenko, H. Rothermel, T. Hagl, V. Fortov, A. Nefedov, V. Molotkov, O. Petrov, A. Lipaev, A. Ivanov, and Y. Baturin, Phys. Plasmas **10**, 1 (2003).
[20]A. Piel, M. Klindworth, and O. Arp, Phys. Rev. Lett. **97**, 205009 (2006).
[21]O. Arp, D. Caliebe, K. O. Menzel, A. Piel, and J. Goree, IEEE Trans. Plasma Sci. **38**, 842 (2010).
[22]M. Rosenberg, J. Vac. Sci. Technol. A **14**, 631 (1996).
[23]G. Joyce, M. Lampe, and G. Ganguli, Phys. Rev. Lett. **88**, 095006 (2002).
[24]P. Epstein, Phys. Rev. **23**, 710 (1924).
[25]R. L. Merlino, Phys. Plasmas **16**, 124501 (2009).
[26]T. Trottenberg, D. Block, and A. Piel, Phys. Plasmas **13**, 042105 (2006).
[27]E. Thomas, Phys. Plasmas **13**, 042107 (2006).
[28]O. Arp, D. Block, M. Klindworth, and A. Piel, Phys. Plasmas **12**, 122102 (2005).
[29]J. B. Pieper, J. Goree, and R. A. Quinn, Phys. Rev. E **54**, 5636 (1996).

[30]K. O. Menzel, O. Arp, and A. Piel, Phys. Rev. Lett. **104**, 235002 (2010).
[31]J. H. Scofield, Am. J. Phys. **62**, 129 (1994).
[32]A. Piel and A. Melzer, Plasma Phys. Controlled Fusion **44**, 201 (2002).
[33]M. Rosenberg and G. Kalman, Phys. Rev. E **56**, 7166 (1997).
[34]P. K. Kaw and A. Sen, Phys. Plasmas **5**, 3552 (1998).
[35]M. S. Murillo, Phys. Plasmas **7**, 33 (2000).
[36]F. Melandsø, Phys. Plasmas **3**, 3890 (1996).
[37]X. Wang, A. Bhattacharjee, and S. Hu, Phys. Rev. Lett. **86**, 2569 (2001).
[38]B. Liu, J. Goree, V. Nosenko, and L. Boufendi, Phys. Plasmas **10**, 9 (2003).
[39]L. S. Frost, Phys. Rev. **105**, 354 (1957).
[40]SIGLO-2D, Version 1.0, Kinema Software, P.O. Box 1147, 236 N. Washington St., Monument, CO 80132.